

# The molecular mechanism of the cyanobacterial bicarbonate importer CmpABCD activated by the intracellular nitrate

Received: 29 April 2025

Accepted: 7 April 2026

Cite this article as: Li, Q.-Y., Li, B., Zhou, R.-Q. *et al.* The molecular mechanism of the cyanobacterial bicarbonate importer CmpABCD activated by the intracellular nitrate. *Nat Commun* (2026). <https://doi.org/10.1038/s41467-026-72153-w>

Qin-Yao Li, Bo Li, Rui-Qian Zhou, Jun-Lu Lv, Wen-Tao Hou, Shu-Jing Han, Yuxing Chen, Yong-Liang Jiang & Cong-Zhao Zhou

We are providing an unedited version of this manuscript to give early access to its findings. Before final publication, the manuscript will undergo further editing. Please note there may be errors present which affect the content, and all legal disclaimers apply.

If this paper is publishing under a Transparent Peer Review model then Peer Review reports will publish with the final article.

---

**The molecular mechanism of the cyanobacterial bicarbonate importer CmpABCD  
activated by the intracellular nitrate**

Qin-Yao Li<sup>1,#</sup>, Bo Li<sup>1,#</sup>, Rui-Qian Zhou<sup>1,#</sup>, Jun-Lu Lv<sup>2</sup>, Wen-Tao Hou<sup>1</sup>, Shu-Jing Han<sup>1</sup>, Yuxing Chen<sup>1\*</sup>, Yong-Liang Jiang<sup>1\*</sup>, Cong-Zhao Zhou<sup>1\*</sup>

<sup>1</sup>Department of Radiology, the First Affiliated Hospital of USTC, and School of Life Sciences, Division of Life Sciences and Medicine, University of Science and Technology of China, Hefei, China.

<sup>2</sup>Department of Environmental Science and Engineering, University of Science and Technology of China, Hefei, China

<sup>#</sup>These authors contributed equally: Qin-Yao Li, Bo Li, Rui-Qian Zhou

\*Correspondence: cyxing@ustc.edu.cn (Y.C.); jyl@ustc.edu.cn (Y.-L.J.); zcz@ustc.edu.cn (C.-Z.Z.)

---

**Abstract**

Maintaining carbon/nitrogen (C/N) metabolic balance is essential for cellular homeostasis, allowing microorganisms to adapt to fluctuating environmental conditions. In the autotrophic cyanobacteria, the C/N balance is achieved through a sophisticated network that coordinates the uptake of inorganic carbon and nitrogen, including the ATP-binding cassette transporters CmpABCD and NRT that import bicarbonate and nitrate, respectively. Notably, both transporters possess an extra C-terminal regulatory domain (CRD) that is fused to one of the nucleotide-binding domains (NBDs). Via structure guided site-directed mutagenesis and bicarbonate transport activity assays, we found that CmpABCD is tightly regulated by the nitrate-binding CRD. At a low intracellular nitrate concentration, CmpBCD adopts an auto-inhibited conformation, in which the CRD locks the two NBDs of CmpC and CmpD. Upon binding to the nitrate, the CRD is released from NBDs and becomes highly flexible, thus restoring the transport activity of CmpABCD. We propose a distinct regulatory mechanism of ABC transporters, which may be broadly applicable to those fused with a regulatory domain. Moreover, these findings combined with previous reports establish a direct link between the inorganic carbon uptake and intracellular nitrate level through an ABC importer, providing a straightforward and economic strategy that coordinates the C/N homeostasis.

## Introduction

Carbon (C) and nitrogen (N) are the two most abundant nutrient elements in living organisms, which constitute the major components of biomacromolecules<sup>1,2</sup>. The homeostasis of carbon and nitrogen metabolism, which is fundamental for all forms of living organisms to acclimate to fluctuating environments, needs to be precisely controlled<sup>3</sup>. As one of the most ancient photosynthetic prokaryotes, cyanobacteria are primary producers and driving forces of the global biogeochemical C/N cycles<sup>4,5</sup>. They have evolved sophisticated mechanisms to finely tune the C/N balance in response to the environmental fluctuations, including general regulation at the transcriptional level and local tuning at the metabolic level.

To enhance the carboxylation efficiency of photosynthesis, cyanobacteria have evolved a CO<sub>2</sub>-concentrating mechanism (CCM), which substantially accumulates CO<sub>2</sub> in the vicinity of the ribulose-1,5-bisphosphate carboxylase/oxygenase RuBisCO<sup>6,7</sup>. The cyanobacterial CCM consists of a self-assembled icosahedral-like microcompartment, termed the carboxysome, and several inorganic carbon (Ci) uptake systems<sup>6</sup>. To date, five Ci-uptake systems that accumulate intracellular bicarbonate have been identified in cyanobacteria, including three bicarbonate importers BicA<sup>8</sup>, SbtAB<sup>9</sup>, and CmpABCD<sup>10</sup>, in addition to two thylakoid-bound complexes NDH-I<sub>3</sub> and NDH-I<sub>4</sub> that convert CO<sub>2</sub> to bicarbonate<sup>11</sup>. Within the carboxysome, bicarbonate is converted to CO<sub>2</sub> by carbonic anhydrase, providing enriched CO<sub>2</sub> for RuBisCO.

The CCM activity is tightly regulated to maintain intracellular C/N balance in response to the fluctuating level of Ci availability<sup>12,13</sup>. Constitutively, the LysR-type transcription factor NdhR globally represses the expression of several genes encoding the Ci-uptake systems under high Ci conditions<sup>14,15</sup>. Upon accumulation of the inducer 2-phosphoglycolate (2-PG), NdhR dissociates from the promoter, thus activating the expression of Ci-utilization genes<sup>16</sup>. In contrast, another LysR-type transcription factor CmpR activates the bicarbonate importer CmpABCD under low Ci conditions<sup>17,18</sup>. In addition to transcriptional regulation, the cyanobacterial CCM is also finely regulated by the PII-like protein SbtB, which acts as a Ci-sensing module that controls the sodium/bicarbonate symporter SbtA in cyanobacteria via binding different adenylyl-nucleotides including the second messengers cAMP and c-di-AMP<sup>19-21</sup>.

CmpABCD is a high-affinity bicarbonate importer induced under low-Ci conditions<sup>10</sup>. It belongs to the ATP-binding cassette (ABC) transporter family and consists of five subunits: the high-affinity substrate-binding protein CmpA that specifically binds extracellular substrate

---

bicarbonate at a  $K_d$  of 5  $\mu\text{M}$ <sup>22</sup>, two identical transmembrane domains (TMDs) CmpB, and two different nucleotide-binding domains (NBDs) in CmpC and CmpD responsible for ATP binding and hydrolysis. Distinct from canonical ABC transporters<sup>23–26</sup>, CmpC possesses an additional C-terminal regulatory domain (CmpC-CRD) fused to its NBD (CmpC-NBD), which shares a sequence identity of ~30% with CmpA. The architecture of CmpABCD closely resembles that of the nitrate ABC transporter NRT<sup>27</sup>, which harbors a conserved CRD domain that allosterically regulates the transport activity of NRT via specific interaction with the signaling protein PII<sup>28</sup>. Notably, CmpC-CRD also shares a sequence identity of ~30% with the nitrate-binding protein NrtA, especially a similar solute-binding pocket and a highly conserved lysine residue binding to the nitrate<sup>29</sup>. It suggests that CmpC-CRD might also bind to nitrate. However, it remains unknown how a nitrate-binding CRD regulates the bicarbonate uptake activity of CmpABCD.

Here, we present the biochemical and structural analyses of CmpBCD, revealing that the CRD indeed specifically binds to nitrate; and moreover, acts as a sensor of intracellular nitrate that finely regulates the conformation of CmpBCD and eventually determines its bicarbonate transport activity. A series of genetic analyses guided by structural analysis clearly show us the molecular insights into the modulation of a bicarbonate importer via sensing the intracellular nitrate level. These findings uncover a distinct regulatory mechanism of ABC transporters as well as a feedback loop that precisely controls the C/N homeostasis in cyanobacteria.

## Results

### CmpC possesses a CRD harboring a conserved nitrate-binding pocket

Similar to previous prediction<sup>29</sup>, our sequence analysis showed that CmpC-CRD possesses a sequence identity of ~30% and ~50% to the nitrate-binding protein NrtA and the CRD of the nitrate importer NRT, respectively, both of which have been proven to bind to nitrate<sup>28</sup>. Moreover, the nitrate-binding residues of NrtA and NrtC-CRD are highly conserved in CmpC-CRD (Fig. 1a), which strongly implies that CmpC-CRD should also bind to nitrate. We therefore performed binding assays of CmpC-CRD towards the bicarbonate and the common nitrogen sources, including nitrate, ammonium, nitrite, glutamine, and urea. As predicted, CmpC-CRD specifically binds to nitrate, at a dissociation constant ( $K_d$ ) of 0.38 mM (Fig. 1b), but not bicarbonate or other nitrogen sources (Supplementary Fig. 1a).

To further elucidate the nitrate-binding mode of CmpC-CRD, we solved the crystal structures of the apo- and nitrate-bound forms of CmpC-CRD at 1.56 and 1.75 Å, respectively (Fig. 1c, d, and Supplementary Fig. 1b). The structure of CmpC-CRD consists of three subdomains, forming a C-clamp shape. Similar to the previously reported structures of NrtA<sup>29</sup> and CmpA<sup>30</sup>, two of the subdomains (lobe I and II) of CmpC-CRD form a substrate-binding cleft, where a nitrate molecule binds (Fig. 1d). Similarly, each lobe consists of a five-stranded mixed  $\beta$ -sheet sandwiched by two  $\alpha$ -helices on each side. In addition, CmpC-CRD also has an additional C-terminal  $\alpha$ -helical subdomain that bridges lobe I and II (Fig. 1c, d). Structural superposition showed that CmpC-CRD closely resembles the NrtC-CRD of NRT<sup>28</sup>, at a root mean square deviation (RMSD) value of 1.11 Å over 310 C $\alpha$  atoms (Supplementary Fig. 1c).

In the nitrate-bound structure, a molecule of nitrate binding to the cleft between lobe I and II is completely occluded from the solvent. The nitrate is stabilized by residues Trp319, His408, Gly452, and Lys481 (Fig. 1d). The O1 atom of nitrate forms a salt bridge with Lys481 and hydrogen bonds with His408 and Gly452, whereas the O2 atom of nitrate makes a hydrogen bond with Trp319 (Fig. 1d). Sequence analysis showed that these nitrate-binding residues are highly conserved among homologs (Fig. 1a). Particularly, the counterpart of Lys481 (corresponding to Lys269 in *Synechocystis* sp. PCC 6803 NrtA and Lys480 in *Anabaena* sp. PCC 7120 NrtC-CRD) was found to complement the negative charge of the O1 atom of nitrate (Supplementary Fig. 1c), therefore determining the substrate specificity<sup>29</sup>. Mutation of Lys481 in CmpC-CRD to alanine significantly reduced its binding affinity towards nitrate, further confirming the critical role of this

lysine residue for nitrate specificity (Supplementary Fig. 1d). In contrast, CmpA harbors a glutamate residue (corresponding to Lys481 in CmpC-CRD) at the bicarbonate-binding pocket (Supplementary Fig. 2a) that acts as a hydrogen-bonding acceptor for the hydroxyl group of the substrate bicarbonate<sup>30</sup>.

Compared to the apo-form CmpC-CRD, the overall structure of nitrate-bound CmpC-CRD exhibits minor conformational changes, with an RMSD value of 0.42 Å over Cα 323 atoms. Consistent with an induced-fit upon nitrate binding, the helices α3 and α8 of CRD that contribute to the interactions with nitrate, shift by ~1 Å toward each other (Supplementary Fig. 2b), therefore narrowing the nitrate-binding pocket and reducing its volume from 243 Å<sup>3</sup> to 47 Å<sup>3</sup> (Supplementary Fig. 2c).

### **CmpABCD is intrinsically inactive due to the presence of CRD**

It was found that expression of *cmpABCD* operon is induced by the transcriptional regulator CmpR under low-Ci conditions<sup>10,18,31</sup>. However, overexpression of *Synechococcus elongatus* PCC 7942 CmpABCD in *E. coli* could not enable the bicarbonate uptake activity<sup>32</sup>. We therefore hypothesize that the constitutive fusion of a CRD to one of the nucleotide-binding domains may inherently retain CmpABCD inactive.

To verify this hypothesis, we expressed CmpABCD from *Pseudanabaena* sp. Chao 1811 in *E. coli* and conducted serial dilution spotting assays. It was known that deletion of the carbonic anhydrase gene *can* in *E. coli* resulted in the incapability of cell growth under normal air conditions<sup>33</sup>, which could be rescued upon the introduction of a bicarbonate importer<sup>32</sup>. Similar to the previous report<sup>32</sup>, the *can*-deleted *E. coli* C43 cells (termed C43-Δ*can*) overexpressing the wild-type CmpABCD could not grow (Fig. 2a). However, deletion of CRD from CmpC enabled the *E. coli* C43-Δ*can* cells to grow, indicating the CRD-deleted CmpABCD possesses the bicarbonate uptake activity (Fig. 2a). We further performed the bicarbonate uptake assays in *Synechocystis* cultured in medium supplemented with 500 μM ammonium, and found that deletion of CRD in *Synechocystis* augmented the bicarbonate uptake activity to ~1.2 folds (Fig. 2b). It suggests that the intrinsically inactive state of CmpABCD is due to the presence of CRD.

### **CmpBCD adopts a constitutively auto-inhibited conformation locked by the CRD**

To explore the structural insights of this intrinsic inactivation, we screened and expressed CmpABCD homologs from various cyanobacterial strains, and finally we obtained the best-behaved CmpBCD from *Pseudanabaena* sp. Chao 1811 (termed *Pseudanabaena* for short) and solved its cryo-EM structure at 3.40 Å resolution (Fig. 3a and Supplementary Fig. 3). The substrate-binding protein CmpA is usually flexibly tethered to the membrane and dynamically interacts with the TMDs; thus, it was not incorporated in our complex. Notably, in the absence of CmpA, CmpBCD retained the capability of binding to the substrate bicarbonate, at a  $K_d$  of 88 μM (Supplementary Fig. 4).

The overall structure of CmpBCD adopts an inward-facing conformation (Fig. 3a). It comprises two identical transmembrane subunits of CmpB forming a putative substrate transport channel, in addition to two various cytoplasmic NBDs: CmpC and CmpD. The two CmpB subunits, each with six TM helices (Fig. 3a), pack against each other and form a swapped dimer with TM1 and TM6 of one subunit extending and interacting with the opposite subunit. Besides six TM helices, CmpB contains three additional α-helices: one is located at the periplasmic side, whereas the other two, including a conserved coupling helix, are located at the cytoplasmic side (Fig. 3a). The CmpC-NBD and CmpD adopt a classical NBD fold of ABC transporter composed of two subdomains (RecA-like and α-helical subdomains) harboring the conserved motifs<sup>34-37</sup>: Walker A, Walker B, and ABC signature motif (Supplementary Fig. 5).

The two NBDs in the "semi-open" dimer interact with each other mainly via the C-terminal α-helices of CmpC and CmpD, accounting for a total interface of ~850 Å<sup>2</sup>. The α-helical subdomains of two NBDs are separated from each other, whereas the TMDs in the inner membrane leaflet open toward the intracellular side, resulting in an inward-facing conformation of CmpBCD. Meanwhile, the TMDs in the outer membrane leaflet remain bundled, with a buried interface area of ~2300 Å<sup>2</sup> through the interactions of TM1 and TM6 of one TMD with TM3 of the opposite TMD (Fig. 3a).

Notably, the cryo-EM map of CmpC-CRD is clearly visible and continuous, which enables us to build the atomic model of CRD at ~3.5 Å resolution (Fig. 3b). The CmpC-CRD structure more closely resembles the apo-form crystal structure, with an RMSD of 0.87 Å against the 330 Cα atoms (Supplementary Fig. 6). In the CmpBCD structure, the CRD simultaneously binds to the two NBDs, with the substrate-binding cleft of CRD facing the hinge helix of CmpC and the α7 helix of CmpD, creating a triangular configuration that locks the NBDs (Fig. 3a). The CRD

interacts with CmpC-NBD via specifically engaging the hinge helix of CmpC, making a total interface area of  $\sim 750 \text{ \AA}^2$  (Fig. 3c). In addition to extensive van der Waals contacts, several salt bridges Arg320-Glu249 and Glu316-Arg259, and hydrogen bonds Gln436-Ser248 and Asp324-Tyr252 further stabilize the interface (Fig. 3c).

On the other side, the CRD interacts with the helices  $\alpha 7$  and  $\alpha 8$  of CmpD, forming an interface area of  $\sim 500 \text{ \AA}^2$  (Fig. 3d). Several polar interactions, including the salt bridges Arg315-Glu255, Lys442-Asp261 and Arg527-Asp249, in addition to a hydrogen bond Thr317-Glu255, are observed to stabilize the interface between CRD and CmpD (Fig. 3d). Moreover, the serial dilution spotting assays showed that the CmpC-R315A&CmpD-E255Q double mutations partially restored the growth of *E. coli* C43- $\Delta can$  (Fig. 2a), further confirming the essential role of residues CmpC-Arg315 and CmpD-Glu255 for the interactions. Similarly, the double mutant CmpC<sub>R315A</sub>&CmpD<sub>E255Q</sub> of *Synechocystis* also gains a bicarbonate uptake activity up to  $\sim 1.4$  folds, compared to the wild type (Fig. 3e). The structural and functional analyses demonstrated that the CRD interacts with two NBDs and locks CmpABCD at a frozen conformation, which abolishes the bicarbonate transport activity under normal conditions.

### **The bicarbonate transport activity of CmpABCD is induced upon the intracellular nitrate binding to CRD**

CmpC possesses an extension of CRD with a specific nitrate-binding cleft, indicating that the nitrate might play a role in regulating the transport activity of CmpABCD. Moreover, the surface plasmon resonance assays confirmed that CmpBCD is capable of binding to nitrate with a  $K_d$  of  $117 \text{ \mu M}$  (Supplementary Fig. 7). We therefore performed the bicarbonate uptake assays in *Synechocystis* to test the role of nitrate on the regulation of CmpABCD activity. Previous reports have shown that ammonium is the most favorite nitrogen source for cyanobacteria growth<sup>28,29</sup>; thus, addition of ammonium in the medium could mimic a nitrate-limited condition. The *Synechocystis* in the presence of nitrate exhibits a bicarbonate uptake activity of  $\sim 2.2$  times that of the cells cultured in ammonium (Fig. 4a). Substitution of the nitrate-binding residue Lys482 with alanine in the CRD dramatically reduces the bicarbonate uptake activity to a basal level (Fig. 4b), indicating that the mutation makes CmpABCD incapable of responding to the availability of nitrate in the medium. These results strongly indicate that the presence of nitrate relieves the auto-inhibition state of CmpABCD, and restores its bicarbonate uptake activity.

To further investigate the regulatory mechanism of nitrate on CmpABCD activity, we expressed and purified *Pseudanabaena* CmpBCD in the presence of 0.8 mM  $\text{NO}_3^-$ , and solved the cryo-EM structure of CmpBCD at 3.39 Å resolution (Fig. 4c and Supplementary Fig. 8). However, the cryo-EM map of CRD is rather dispersed with some segments at a resolution up to ~5.5 Å, preventing the building of an atomic model (Fig. 4c). The lower resolution of CRD reflects the increased flexibility relative to the core structure in the presence of nitrate, causing its density averaged during cryo-EM data processing. It also suggests that the presence of nitrate may dissociate the CRD from the NBDs, making it highly flexible. Besides the dynamic CRD, the core structure of CmpBCD also adopts an inward-facing conformation, which closely resembles the auto-inhibited structure of CmpBCD, with an RMSD value of 0.49 Å over 954 C $\alpha$  atoms (Fig. 4d). The main difference between the two structures lies in the movement of the hinge helix of CmpC (Fig. 4d). In the auto-inhibited conformation, the hinge helix is positioned close to and interacts with the CRD. In contrast, in CmpBCD structure in the presence of nitrate, the hinge helix tightly packs against both CmpD and CmpC-NBD (Fig. 4d).

Structural analysis showed that in the absence of nitrate, the CRD adopts a conformation that favors its binding to the two NBDs, thereby locking CmpBCD in an auto-inhibited conformation (Fig. 3a). Structural superposition of CRD from the apo-CmpBCD cryo-EM structure with the apo-CRD and CRD- $\text{NO}_3^-$  crystal structures yielded RMSD values of 0.87 Å and 0.95 Å, respectively, indicating that CRD in apo-CmpBCD more closely resembles the apo-CRD crystal structure (Supplementary Fig. 6). Superposition of CRD- $\text{NO}_3^-$  crystal structure onto that in apo-CmpBCD further showed that nitrate binding drives lobes I and II of CRD to move toward each other, from 8.1 Å to 6.2 Å, which alters their interfaces with the two NBDs (Fig. 4d and Supplementary Fig. 9). Particularly, upon nitrate binding to the inter-domain cleft of CRD, the residues Asn436 and Arg527 at the CRD-NBDs interfaces shift slightly toward nitrate but away from the NBDs. This conformational change makes the CRD dissociated from the NBDs.

### **A proposed activation model of CmpABCD**

To further capture the different catalytic state of CmpBCD, we mutated the catalytic glutamate residues (CmpC-Glu164 and CmpD-Glu170) in two NBDs to glutamine, and pre-incubated ATP and the substrate bicarbonate with the purified CmpBCD. Eventually, we solved

the cryo-EM structure of CmpBCD in complex with ATP at 3.15 Å resolution, with the CRD invisible in the cryo-EM map (Fig.5a and Supplementary Fig. 10).

In the structure, two ATP-Mg<sup>2+</sup> molecules symmetrically bind to the cleft between the Walker A motif of one NBD and the ABC signature motif of the other, triggering the closure of the NBD dimer. This conformational change in the NBDs is further transmitted to TMDs via a pair of coupling helices, reducing the distance between the two coupling helices from 25.4 to 13.3 Å (Fig. 5b). Consequently, the TMDs in the inner membrane leaflet move closer to each other, whereas the two TM5 helices in the outer membrane leaflet undergo an outward shift of 10.9° relative to the central axis (Fig. 5b). These coordinated movements result in complete closure of TMDs at the cytoplasmic gate. Moreover, calculation of the substrate translocation channel in the TMDs using the program CAVER 3.0<sup>38</sup> shows that the periplasmic gate is sealed by surrounding residues (Supplementary Fig. 11a, b), which is insufficient to permit substrate translocation. Therefore, the CmpBCD-ATP structure is assigned as an occluded conformation, representing an intermediate state in which the TMDs are oriented toward the periplasm while the periplasmic gate remains sealed. Consistently, although 20 mM NaHCO<sub>3</sub> was included in the cryo-EM sample preparation buffer, no density corresponding to the substrate bicarbonate is observed in the CmpBCD-ATP structure, likely due to the occluded conformation that precludes substrate engagement.

Based on structural and functional data, we propose a putative model for the transport of cyanobacterial CmpABCD (Fig. 6). CmpABCD constitutively adopts an auto-inhibited inward-facing conformation in the absence of nitrate, which is stabilized by CRD simultaneously binding to both CmpC-NBD and CmpD. Upon the accumulation of intracellular nitrate, binding to nitrate enables CRD to release from the two NBDs and therefore activates the bicarbonate transport activity of CmpABCD. During the transport cycle, ATP binding induces dimerization of the NBDs, prompting the TMDs to undergo pronounced conformational changes, which adopt an occluded, and subsequently an outward-facing conformation that is accessible to the bicarbonate. Following ATP hydrolysis, the two NBDs separate, triggering a return to the inward-facing conformation that promotes the release of bicarbonate into the cytoplasm.

## Discussion

### **CmpABCD possesses a distinct regulatory mode of ABC transporters**

Many ABC transporters contain additional regulatory domains fused to the NBDs that function to regulate the transport activity via sensing the small molecules or the partner proteins<sup>39</sup>. For example, the molybdate transporter ModBC<sup>40</sup> and the methionine transporter MetNI<sup>41</sup> have a trans-inhibition mechanism, in which the substrate at high concentration binds to the regulatory domains and inhibits the ATPase activity, locking the transporter at an inward-facing conformation<sup>40</sup>. The glycine betaine transporter OpuA is inhibited under low-osmotic conditions through dimerization of its intracellular cyclic-di-AMP binding domains<sup>25</sup>. Additionally, the polyamine transporter PotABC is stabilized at an inactive conformation upon the substrate binding to the regulatory domains<sup>42</sup>.

In contrast to these regulatory domains symmetrically fused to the NBDs, CmpABCD has only one CRD domain that is fused to the C-terminus of CmpC. The CRD functions as a regulatory sensor that finely tunes the bicarbonate transport activity of CmpABCD via sensing the intracellular nitrate level. In the absence of nitrate, CmpABCD is auto-inhibited via the CRD locking the NBDs. Upon the accumulation of intracellular nitrate, the CRD in complex with nitrate is released from the NBDs, eventually restoring the transport activity, which differs from the trans-inhibition via the regulatory domains binding to the substrates of ModBC<sup>40</sup> and MetNI<sup>41</sup>. Consistently, the addition of nitrate indeed stimulates the ATPase activity of CmpBCD, yielding an  $EC_{50}$  of 4.49 mM (Supplementary Fig. 12a). Moreover, addition of nitrate to these non-inhibited mutants does not stimulate any significant increase of the ATPase activity (Supplementary Fig. 12b). However, the bona fide substrate bicarbonate has no effect on the stimulation of activity of CmpBCD, even in the presence of CmpA (Supplementary Fig. 12c), most likely due to the relatively small size of bicarbonate.

Notably, the overall structure of CmpABCD closely resembles the nitrate importer NRT<sup>28</sup>, both of which have an additional CRD domain that specifically binds to the nitrate. The two core structures (TMDs and NBDs) are nearly identical, with an RMSD value of 1.10 Å over 974 C $\alpha$  atoms (Supplementary Fig. 13a). Moreover, the substrate translocation channel in the TMDs is highly conserved particularly for the conserved residues Arg129, Leu134, Arg210 and Leu218 in CmpB (Supplementary Fig. 13b). The counterparts of these residues in NRT were confirmed to be indispensable for substrate recognition<sup>28</sup>. To further test the role of these residues in CmpB, we

conducted mutations of Leu134, Leu218 and Arg129 to alanine and performed the ATPase activity assays using the CRD-deleted CmpBCD. The results showed that these mutants no longer respond to the substrate bicarbonate (Supplementary Fig. 13c). These results suggest that CmpABCD and NRT share a similar substrate-binding pattern in the corresponding TMDs. However, the regulatory mechanisms of CmpABCD and NRT differ a lot. In CmpABCD, the CRD binds to nitrate, serving as a sensor of intracellular nitrogen status. Although the CRD in NRT could also bind to nitrate, it primarily functions as a hub to interact with the signaling protein PII, but not a nitrate sensor. In this case, PII senses the intracellular C/N status via the signal molecule 2-oxoglutarate (2-OG), thereby modulating the nitrate transport activity of NRT<sup>16,28,43</sup>. Moreover, the CRDs of the two importers interact with the NBDs in distinct modes (Supplementary Fig. 13d). The CRD of CmpBCD interacts with both NBDs and locks the NBDs in an auto-inhibited state. In contrast, the CRD of NRT only contacts the NBD of NrtC, creating a platform to recruit PII<sup>28</sup>.

### **A bicarbonate importer directly senses the intracellular nitrate to maintain the C/N homeostasis in cyanobacteria**

The metabolism of carbon and nitrogen is tightly coupled to maintain the homeostasis for cell growth<sup>44,45</sup>. Cyanobacteria can efficiently absorb and assimilate CO<sub>2</sub> through CCMs, which rely on several inorganic carbon importers. Among these, the high-affinity bicarbonate importer CmpABCD<sup>8-10</sup> is not only tightly regulated at the transcriptional level by CmpR<sup>18</sup>, but also stringently controlled at the activity level. In addition, cyanobacteria utilize different kinds of nitrogen sources, including ammonium, nitrate/nitrite, and nitrogen, with ammonium being the most preferred<sup>46</sup>. When ammonium is abundant, it not only inhibits nitrate uptake, but also halts nitrate utilization by inhibiting the nitrate reductase<sup>47</sup>.

Together with previous reports<sup>10,29,30</sup>, our findings enable us to propose a molecular mechanism in which nitrate directly regulates the bicarbonate transport activity of CmpABCD, thus maintaining the C/N balance in cyanobacteria. When the intracellular nitrogen sources (e.g., ammonium, nitrate, nitrite) are limited (high C/N ratio), the central metabolite 2-OG accumulates and binds to PII, leading to its release from the nitrate importer NRT, thereby activating nitrate uptake. The resulting increase in intracellular nitrate levels restores the C/N balance in cyanobacteria. Meanwhile, the low intracellular nitrate concentration keeps the bicarbonate transporter CmpABCD in an auto-inhibited state, reducing bicarbonate uptake and lowering

intracellular carbon levels, which also contributes to restoring C/N balance. In contrast, when intracellular nitrogen is abundant (low C/N ratio), excess ammonium inhibits nitrate reduction, resulting in intracellular nitrate accumulation. The elevated intracellular nitrate binds to CmpC-CRD, causing its dissociation from the NBDs and relieving the auto-inhibition of CmpABCD. Activated CmpABCD then enhances bicarbonate transport, increasing intracellular carbon levels. At the same time, PII binds to NRT and specifically represses its transport activity, which further restricts nitrate uptake and prevents excessive accumulation<sup>28,43</sup>. Notably, as CmpABCD is a high-affinity bicarbonate importer<sup>31</sup>, the model presented here may be particularly relevant under conditions of low bicarbonate and nitrate concentrations, which are commonly found in the natural habitats of cyanobacteria<sup>48</sup>. The intracellular nitrate level acts as the feedback regulator to finely tune the carbon and nitrogen assimilation pathways in cyanobacteria.

Notably, *in vitro* addition of ATP alone stabilizes the majority of CmpBCD particles in an occluded conformation, which appears to be inconsistent with *in vivo* functional assays showing that nitrate is indispensable for activating the CmpABCD activity. This discrepancy likely arises from the differences in experimental conditions. *In vitro* purification of CmpBCD complex requires detergents to mimic the native membrane environment. However, the stability of CmpBCD in detergent-containing solutions is strongly influenced by ionic strength. Consistent with this, cryo-EM data analyses revealed conformational heterogeneity of the *in vitro* purified CmpBCD complex samples. In the apo-CmpBCD sample, ~85% of the particles exhibit stable CRD-NBD interactions, whereas the CRD is relatively flexible in ~15% of the particles (Supplementary Fig. 3a). Similarly, in the CmpBCD-ATP dataset, approximately 86% of the particles exhibit a flexibly tethered CRD, whereas only ~14% retain stable CRD-NBD interactions (Supplementary Fig. 10a). Structural analysis indicated that the CRD-NBD interface is predominantly hydrophilic (Fig. 3c, d), rendering it susceptible to disruption under elevated ionic conditions. Taken together, these results indicate that high ionic strength during *in vitro* purification partially destabilizes the CRD-NBD interface, allowing ATP binding alone to stabilize a majority of particles in an occluded conformation, even in the absence of nitrate.

Taken together, we elucidate the fine mechanism of how the nitrate regulates the bicarbonate uptake by CmpABCD to maintain the C/N homeostasis in cyanobacteria. These findings establish a direct molecular link between inorganic carbon uptake and nitrogen availability through an ABC transporter, providing a direct feedback loop between carbon and nitrogen assimilation pathways.

---

We also propose a distinct regulatory mode of ABC transporters, in which one CRD domain binds to two NBDs and auto-inhibits its transport activity.

ARTICLE IN PRESS

## Methods

### Protein expression and purification

The *cmpBCD* gene cluster from *Pseudanabaena* sp. Chao 1811 was amplified by PCR and cloned into pET19b expression vector with a C-terminal 3 × Flag tag (DYKDHDGDYKDHDIDYKDDDDK) fused to CmpC using the ClonExpress™ II One Step Cloning Kit (C112-02, Vazyme Biotech Co., Ltd.). Site-directed mutagenesis was performed by a standard two-step PCR protocol. All constructs were verified by sequencing (Sangon Biotech, Shanghai).

Protein expression was performed in *E. coli* C43(DE3) cells cultured in LB medium supplemented with 60 µg/mL ampicillin at 37°C. When the optical density at 600 nm (OD<sub>600</sub>) reached ~0.8, protein expression was induced by adding 0.3 mM isopropyl-β-D-thiogalactopyranoside (IPTG), followed by incubation at 37°C for 4 hr. Cells were harvested by centrifugation and resuspended in lysis buffer (20 mM TES, pH 7.5, 100 mM NaCl, 20% glycerol). Cell lysis was performed using an AH-1500 High-Pressure Homogenizer (ATS Inc.) with 10 passes at ~700 bar. The lysate was centrifuged at 17,300 × *g* for 30 min at 4°C to remove cell debris. The supernatant was further ultracentrifuged at 148,742 × *g* (Beckman, Type 70 Ti rotor) for 1 hr at 4°C to pellet the membrane fraction, which was resuspended in lysis buffer, snap-frozen in liquid nitrogen, and stored at -80°C.

For membrane protein purification, the membrane suspension was solubilized with 1% (w/v) lauryl maltose neopentyl glycol (LMNG, NG310, Anatrace) and 0.5% (w/v) n-dodecyl-β-D-maltopyranoside (DDM, Bluepus) by gentle rotation at 4°C for 2 hr. Insoluble materials were removed after ultracentrifugation at 148,742 × *g* (Beckman, Type 70 Ti rotor) for 45 min, and the supernatant was incubated with anti-FLAG M2 affinity gel (Sigma-Aldrich) on ice for 1 hr. The resin was washed sequentially with 5 mL aliquots of buffer containing 20 mM TES, pH 7.5, 100 mM NaCl, 0.02% (w/v) glyco-diosgenin (GDN, GDN101, Anatrace), and a gradient of glycerol (20%, 15%, 10%, 5%, and 0% (v/v)). Bound protein was eluted using a buffer containing 20 mM TES, pH 7.5, 100 mM NaCl, 0.02% GDN, and 200 µg/mL FLAG peptide. The eluate was concentrated using a 100-kDa molecular weight cut-off centrifugal filter (Millipore), and further purified by size-exclusion chromatography (Superdex 200 Increase 10/300 GL, Cytiva) in buffer containing 20 mM TES, pH 7.5, 100 mM NaCl, and 0.02% GDN. The same expression and purification procedures were used for all mutant constructs.

The gene encoding CmpC-CRD was PCR-amplified from *Pseudanabaena* sp. Chao 1811 and cloned into the pET28a expression vector with a C-terminal 6 × His tag using the ClonExpress™ II One Step Cloning Kit (C112-02, Vazyme Biotech Co., Ltd.). Expression was performed in *E. coli* BL21(DE3) cells grown in LB medium supplemented with 45 µg/ml kanamycin at 37°C with shaking. At OD<sub>600</sub> of ~0.8, expression was induced with 0.3 mM IPTG and continued overnight at 16°C for 21 hr. Cells were harvested by centrifugation and resuspended in lysis buffer (20 mM Na<sub>2</sub>HPO<sub>4</sub>, pH 8.0, 300 mM NaCl, 10% glycerol). Following sonication on ice and centrifugation, the supernatant was loaded onto Ni-NTA affinity resin (Qiagen). The column was washed with buffer containing 20 mM Na<sub>2</sub>HPO<sub>4</sub>, pH 8.0, 300 mM NaCl, 20 mM imidazole, and the protein was eluted with buffer containing 20 mM Na<sub>2</sub>HPO<sub>4</sub>, pH 8.0, 100 mM NaCl, 400 mM imidazole. The eluate was further purified by size-exclusion chromatography on a HiLoad™ Superdex™ 75 pg column (Cytiva) equilibrated in 20 mM Na<sub>2</sub>HPO<sub>4</sub>, pH 8.0, 100 mM NaCl. The CRD-NO<sub>3</sub><sup>-</sup> complex was purified following the same protocol as apo-CRD, with buffer supplemented with 10 mM NaNO<sub>3</sub>. Site-directed mutants of CmpC-CRD were generated by PCR-based mutagenesis and purified following the same protocol as the wild-type proteins.

### **Cryo-EM sample preparation and data collection**

For the apo-CmpBCD sample, 3.5 µL aliquots of purified CmpBCD protein at a concentration of ~5 mg/mL were applied to glow-discharged QUANTIFOIL Au grids (R1.2/1.3, 300 mesh, holey carbon films). The grids were blotted for 6 sec at a blotting force of -2 using filter paper and subsequently plunge-frozen in liquid ethane cooled by liquid nitrogen with a Vitrobot Mark IV (Thermo Fisher Scientific) at 100% humidity and 4°C. A total of 3,036 micrograph stacks were automatically collected using EPU 2.0 software<sup>49</sup> on a Titan Krios G3i microscope operating at 300 kV, equipped with a K3 direct electron detector (Gatan) and a GIF Quantum energy filter (Gatan). Data were acquired at a nominal magnification of ×81,000, with defocus values ranging from -2.3 to -1.5 µm. Motion correction and dose weighting were performed using patch motion correction with a Fourier cropping factor of 0.5, yielding a pixel size of 1.07 Å. Defocus values were estimated using Patch contrast transfer function (CTF) estimation<sup>50</sup>.

For the CmpBCD-NO<sub>3</sub><sup>-</sup> sample, purified CmpBCD protein at a concentration of ~5 mg/mL was mixed with 800 µM NaNO<sub>3</sub>, and 3.5 µL aliquots of the mixture were applied to glow-discharged QUANTIFOIL Au grids (R 1.2/1.3, 300 mesh, holey carbon films). The grids were

blotted for 6 sec at a blotting force of -2 and plunge-frozen in liquid ethane using a Vitrobot Mark IV under the same conditions as described above. A dataset comprising 922 micrograph stacks was collected under the same conditions as the apo-CmpBCD sample. Motion correction and dose weighting were performed using patch motion correction with a Fourier cropping factor of 0.5, yielding a pixel size of 1.07 Å. Defocus values were estimated using Patch CTF estimation.

For the CmpBCD-ATP sample, purified CmpBC<sub>E164Q</sub>D<sub>E170Q</sub> protein at a concentration of ~5 mg/mL was mixed with 10 mM ATP-Mg<sup>2+</sup> and 20 mM NaHCO<sub>3</sub>, followed by incubation on ice for 60 min. 3.5 µL aliquots of protein mixture were applied to glow-discharged QUANTIFOIL Au grids (R 1.2/1.3, 300 mesh, holey carbon films). The grids were blotted for 6 sec at a blotting force of -2 and plunge-frozen in liquid ethane using a Vitrobot Mark IV under the same conditions as described above. A dataset comprising 3,788 micrograph stacks was collected under identical conditions as the apo-CmpBCD sample. Motion correction and dose weighting were performed using MotionCor2<sup>51</sup> with a binning factor of 2, resulting in a pixel size of 1.07 Å. Defocus values were estimated using CTFFIND4<sup>52</sup>.

### Image processing

For the apo-CmpBCD dataset, a total of 2,123,188 particles were automatically picked from 3,036 micrographs using cryoSPARC 3.1<sup>50</sup>. After 2D classification, 494,628 particles were selected for ab initio reconstruction followed by heterogeneous refinement under C1 symmetry. The final subset of 210,668 particles was utilized for homogeneous reconstruction, non-uniform refinement, and local refinement, yielding a final reconstruction map at a global resolution of 3.40 Å.

For the CmpBCD-NO<sub>3</sub><sup>-</sup> dataset, a total of 665,840 particles were automatically picked from 922 micrographs using cryoSPARC 3.1. After 2D classification, 148,318 particles were selected for ab initio reconstruction followed by heterogeneous refinement under C1 symmetry. The resulting 97,237 particles were subjected to iterative processing including homogeneous reconstruction, non-uniform refinement, and local refinement, yielding a final reconstruction map at a global resolution of 3.39 Å.

For the CmpBCD-ATP dataset, a total of 3,408,568 particles were automatically picked from 3,788 micrographs using RELION 3.1<sup>53</sup>. These particles were subjected to reference-free 2D classification, from which 1,639,839 particles from high-quality classes were selected. The

selected particles were subjected to multiple rounds of global angular search 3D classification under C1 symmetry, resulting in four distinct classes. A total of 528,820 particles from the best classes were merged and further refined using 3D refinement with a customized mask, achieving a reconstruction map at a global resolution of 3.15 Å. Subsequent processing included CTF refinement and Bayesian polishing to improve map quality.

The resolutions of all cryo-EM maps were determined by the Fourier shell correlation (FSC) at 0.143 criterion<sup>54</sup>.

### Model building and refinement

The final sharpened map of the CmpBCD-ATP complex, with a B-factor of -115.63 Å<sup>2</sup>, was used for model building in Coot<sup>55</sup>. The high-quality electron density in TMDs enabled unambiguous residue assignment, permitting the manual construction of the TMD models in Coot. The NBDs of CmpC and CmpD were generated using the SWISS-MODEL server<sup>56</sup> and subsequently docked into the 3.15 Å map of CmpBCD-ATP using UCSF ChimeraX<sup>57</sup>. ATP-Mg<sup>2+</sup> molecules were manually built into the corresponding density maps. Real-space structural refinements were performed in PHENIX<sup>58</sup>, with secondary structure and geometry restraints applied to prevent overfitting. For the apo-CmpBCD and CmpBCD-NO<sub>3</sub><sup>-</sup> complexes, models were generated by rigid-body fitting of the CmpBCD-ATP structure, followed by manual refinement. These models were also subjected to real-space refinement in PHENIX.

All structures were validated using PHENIX and MolProbity<sup>59</sup> to ensure the accuracy and quality. Detailed refinement and validation statistics are provided in Supplementary Table 1. Structural figures were prepared with UCSF ChimeraX and PyMOL (<https://pymol.org>).

### Crystallization and structure determination

Crystals of apo-CRD and CRD-NO<sub>3</sub><sup>-</sup> were grown at 16°C using the sitting-drop vapor diffusion method. A mixture of 1 µL of protein solution (10 mg/mL) and 1 µL of reservoir solution (0.1 M Tris, pH 8.0, 12% (w/v) polyethylene glycol 20,000 and 0.1 M Tris, pH 8.0, 0.1 M KCl, 15% (w/v) polyethylene glycol monomethyl ether 2000) was used for crystallization. Single-crystal X-ray diffraction measurements of CRD-NO<sub>3</sub><sup>-</sup> were performed on an XtaLAB PRO

diffractometer at 1.5406 Å and 100 K using Cu X-rays generated by an MMF007 rotating-anode X-ray (Rigaku, Japan) with a Pilatus 200K detector at the Core Facility Center for Life Sciences, USTC. X-ray diffraction data of apo-CRD were collected at 100 K under a liquid nitrogen stream using beamline 02U1 equipped with an EIGER2 S 9M detector at the Shanghai Synchrotron Radiation Facility (SSRF). The diffraction data were integrated and scaled using XDS<sup>60</sup>.

The crystal structure of CmpC-CRD was determined by molecular replacement using the structure of CmpC-CRD from apo-CmpBCD as a search model. The structure was refined using the maximum likelihood method implemented in REFMAC5<sup>61</sup> as part of the CCP4i<sup>62</sup> program suite. Iterative model rebuilding in Coot was followed by further refinement with PHENIX<sup>58</sup>. The final model exhibited excellent geometry and was validated using MolProbity<sup>59</sup>. The volumes of the nitrate-binding pockets of CRD at different states were calculated using Proteins Plus<sup>63</sup>. A list of the parameters of data collection, processing, structure determination, and refinement is provided in Supplementary Table 2.

### ATPase activity assays

The ATPase activity of CmpBCD was measured using a modified malachite green ammonium molybdate method<sup>64</sup>. Reactions were performed in 96-well plates, and absorbance was measured at 630 nm. To assess the effect of nitrate on the ATPase activity, CmpBCD was added at a final concentration of 0.2 μM to a reaction buffer containing 20 mM TES, pH 7.5, 100 mM NaCl, 2 mM MgCl<sub>2</sub>, and 0.02% (w/v) GDN. Nitrate was diluted to the indicated concentrations, and the total reaction volume was adjusted to 100 μL per well. Reactions were initiated by adding ATP to a final concentration of 3 mM, followed by incubation at 37°C for 30 min.

Enzymatic reactions were terminated by adding 25 μL of freshly prepared malachite green development solution. After incubation at room temperature for 2 min to stabilize the chromophore, 10 μL of 10% (w/v) oxalic acid was added to each well. Following a further 60 minutes of incubation, absorbance was measured at 630 nm using a SpectraMax iD5 Multi-Mode Microplate Reader (Molecular Devices). Inorganic phosphate concentrations were determined using a KH<sub>2</sub>PO<sub>4</sub> standard curve. The malachite green development solution was freshly prepared before each experiment by mixing 10 mL malachite green dye stock solution, 2.5 mL of 7.5% (w/v) ammonium molybdate, and 0.2 mL Tween-20. All data represented the mean ± standard deviation (SD) of three independent biological replicates ( $n = 3$ ).

### **Isothermal titration calorimetry assays**

Isothermal titration calorimetry (ITC) experiments were conducted at 13°C using either PEAQ-ITC or ITC200 calorimeter (MicroCal). All measurements were conducted in a buffer containing 20 mM Na<sub>2</sub>HPO<sub>4</sub>, pH 8.0, and 100 mM NaCl. For titration experiments, 51 μM of purified CmpC-CRD was titrated with 20 mM NaNO<sub>3</sub>; 105 μM of CmpC-CRD<sub>K481A</sub> mutant was titrated with 10 mM NaNO<sub>3</sub>; and 51 μM CmpC-CRD was titrated with 10 mM NaHCO<sub>3</sub>. Each titration consisted of 20 injections of 2 μL ligand solution into the 300 μL sample cell, with constant stirring at 750 rpm. Raw data were processed and binding isotherms were fitted using one-set-of-sites model in the MicroCal PEAQ-ITC Analysis Software (Malvern Panalytical).

### **Surface plasmon resonance assays**

All surface plasmon resonance (SPR) experiments were performed on a Biacore 8000 instrument (Cytiva) at 25°C in buffer of 20 mM TES, pH 7.5, 100 mM NaCl and 0.02% GDN. The purified CmpBCD was covalently immobilized onto the series CM5 sensor chips (Cytiva) by amine coupling chemistry. Different concentrations of bicarbonate or nitrate in the running buffer were serially flowed over the chip surface with the immobilized protein and the blank for 1 min at a flow rate of 30 μl min<sup>-1</sup>. The data were fitted with steady-state affinity binding model using Biacore Insight Evaluation software. The graphs were plotted using GraphPad Prism 8 software.

### **Dilution spotting assays**

Chromosomal deletion of the *can* operon in *E. coli* was achieved by cloning PCR-amplified upstream and downstream flanking regions of the *can* operon into the pRE112 vector. The resulting recombinant plasmid (pRE112-Δ*can*) was transformed into *E. coli* C43(DE3), and homologous recombination was induced by culturing in LB medium containing 5% (w/v) sucrose (without NaCl or antibiotics). The deletion mutants were verified by colony PCR and DNA sequencing (Sangon Biotech, Shanghai).

For the dilution spotting assays<sup>32</sup>, *E. coli* C43(DE3) and C43(DE3)-Δ*can* strains carrying various plasmid constructs were first cultured overnight in LB medium supplemented with 75 μg/mL spectinomycin and 0.1 mM sodium azide at 37°C. Overnight cultures were diluted to an OD<sub>600</sub> of 0.6 and subjected to a 10-fold serial dilution series (10<sup>1</sup>-10<sup>5</sup>). Aliquots of 2 μL from each

dilution were spotted onto LB agar plates containing 0.2 mM IPTG and 75 µg/mL spectinomycin, followed by incubation at 37°C overnight. All assays were performed with at least three independent biological replicates.

### Construction of cyanobacterial mutants

To generate the *cmpCD* deletion mutant ( $\Delta$ *cmpCD*) in *Synechocystis* sp. PCC 6803, a 1,000-bp upstream flanking region of the *cmpC* gene, the streptomycin resistance gene, and a 1,000-bp downstream flanking region of the *cmpD* gene were amplified by PCR and assembled into the pGEM-T Easy vector using the NEBuilder Hi-Fi DNA Assembly Master Mix (NEB, E2621S). The resulting plasmid was transformed into wild-type *Synechocystis* sp. PCC 6803 by natural transformation. Transformants were selected on BG11 agar plates containing 15 µg/mL streptomycin and incubated at 30°C under continuous illumination at 30 µmol photons m<sup>-2</sup> s<sup>-1</sup>. The  $\Delta$ *cmpCD* mutants were verified by colony PCR and DNA sequencing.

For constructing site-directed *cmpCD* mutants in the  $\Delta$ *cmpCD* background, a 1,000-bp upstream flanking region of the *cmpC* gene, the kanamycin resistance cassette, a PCR-assembled point-mutated *cmpCD* sequence (generated by overlap extension PCR), and a 1,000-bp downstream region of the *cmpD* were cloned into the pGEM-T Easy vector. The assembled plasmid was transformed into the  $\Delta$ *cmpCD* strain of *Synechocystis* sp. PCC 6803. Transformants were selected on BG11 agar plates supplemented with 15 µg/mL kanamycin under the same growth conditions. Correct integration of the constructs was confirmed by colony PCR and DNA sequencing.

### Bicarbonate uptake assays

Wild-type and mutant strains of *Synechocystis* sp. PCC 6803 were cultured in BG11 medium at 30°C under continuous illumination at 30 µmol photons m<sup>-2</sup> s<sup>-1</sup>. When the optical density at 750 nm (OD<sub>750</sub>) reached approximately 1.5, cells were harvested by centrifugation at 1,900 × g for 5 min and washed twice with nitrogen-free BG11 medium. The washed cells were then resuspended in nitrogen-free BG11 medium supplemented with either 20 mM NaNO<sub>3</sub> (nitrate condition) or 10 mM NH<sub>4</sub>Cl (ammonium condition), and the OD<sub>750</sub> was adjusted to 1.5. Bicarbonate uptake assays were performed by adding NaH<sup>14</sup>CO<sub>3</sub> to a final concentration of 100 µM<sup>22</sup>, followed by incubation for 2 min. The reaction was terminated by rapid filtration through a glass fiber filter (GF/F, Whatman). Filters were immediately washed five times with 1 mL of BG11 medium per wash to

remove unincorporated radiolabel. Radioactivity retained on the filters was quantified using a liquid scintillation counter (Tri-Carb 2910TR, PerkinElmer). Data are presented as the mean  $\pm$  SD of three independent biological replicates ( $n = 3$ ).

### **Data availability**

The cryo-EM density maps of three structures have been deposited at the Electron Microscopy Data Bank under accession codes EMD-63973 [<https://www.ebi.ac.uk/pdbe/entry/emdb/EMD-63973>] (apo-CmpBCD), EMD-63974 [<https://www.ebi.ac.uk/pdbe/entry/emdb/EMD-63974>] (CmpBCD-NO<sub>3</sub><sup>-</sup>), and EMD-63975 [<https://www.ebi.ac.uk/pdbe/entry/emdb/EMD-63975>] (CmpBCD-ATP). And the coordinates have been deposited in the Protein Data Bank (PDB) under accession codes 9U9Z [<https://doi.org/10.2210/pdb9U9Z/pdb>] (apo-CmpBCD), 9UA0 [<https://doi.org/10.2210/pdb9UA0/pdb>] (CmpBCD-NO<sub>3</sub><sup>-</sup>), and 9UA1 [<https://doi.org/10.2210/pdb9UA1/pdb>] (CmpBCD-ATP). The coordinates of two crystal structures have been deposited in PDB under accession codes 9UAK [<https://doi.org/10.2210/pdb9UAK/pdb>] (apo-CRD) and 9UAI [<https://doi.org/10.2210/pdb9UAI/pdb>] (CRD-NO<sub>3</sub><sup>-</sup>). Source data are provided with this paper. The coordinates used in this study are available in the PDB under accession code 2G29 [<https://www.rcsb.org/structure/2G29>] (NrtA-NO<sub>3</sub><sup>-</sup>), 8WM7 [<https://www.rcsb.org/structure/8WM7>] (NrtBCD-P II), and 8WM8 [<https://www.rcsb.org/structure/8WM8>] (NrtBCD-NO<sub>3</sub><sup>-</sup>).

## References

1. Anderson, T. R., Boersma, M. & Raubenheimer, D. Stoichiometry: Linking Elements to Biochemicals. *Ecology* **85**, 1193–1202 (2004).
2. Sardans, J., Rivas-Ubach, A. & Peñuelas, J. The elemental stoichiometry of aquatic and terrestrial ecosystems and its relationships with organismic lifestyle and ecosystem structure and function: a review and perspectives. *Biogeochemistry* **111**, 1–39 (2012).
3. Sardans, J., Rivas-Ubach, A. & Peñuelas, J. The C:N:P stoichiometry of organisms and ecosystems in a changing world: A review and perspectives. *Perspectives in Plant Ecology, Evolution and Systematics* **14**, 33–47 (2012).
4. Glover, H. E., Campbell, L. & Prézelin, B. B. Contribution of *Synechococcus* spp. to size-fractioned primary productivity in three water masses in the Northwest Atlantic Ocean. *Mar. Biol.* **91**, 193–203 (1986).
5. Flombaum, P. *et al.* Present and future global distributions of the marine Cyanobacteria *Prochlorococcus* and *Synechococcus*. *Proc. Natl Acad. Sci.* **110**, 9824 (2013).
6. Price, G. D., Badger, M. R., Woodger, F. J. & Long, B. M. Advances in understanding the cyanobacterial CO<sub>2</sub>-concentrating-mechanism (CCM): functional components, Ci transporters, diversity, genetic regulation and prospects for engineering into plants. *J. Exp. Bot.* **59**, 1441–1461 (2008).
7. Raven, J. A., Beardall, J. & Sánchez-Baracaldo, P. The possible evolution and future of CO<sub>2</sub>-concentrating mechanisms. *J. Exp. Bot.* **68**, 3701–3716 (2017).
8. Price, G. D., Woodger, F. J., Badger, M. R., Howitt, S. M. & Tucker, L. Identification of a SulP-type bicarbonate transporter in marine cyanobacteria. *Proc. Natl Acad. Sci.* **101**, 18228–18233 (2004).
9. Shibata, M. *et al.* Genes Essential to Sodium-dependent Bicarbonate Transport in Cyanobacteria. *J. Biol. Chem.* **277**, 18658–18664 (2002).
10. Omata, T. *et al.* Identification of an ATP-binding cassette transporter involved in bicarbonate uptake in the cyanobacterium *Synechococcus* sp. strain PCC 7942. *Proc. Natl Acad. Sci.* **96**, 13571–13576 (1999).
11. Rae, B. D., Long, B. M., Badger, M. R. & Price, G. D. Functions, Compositions, and Evolution of the Two Types of Carboxysomes: Polyhedral Microcompartments That Facilitate CO<sub>2</sub> Fixation in Cyanobacteria and Some Proteobacteria. *Microbiol. Mol. Biol. Rev.* **77**, 357 (2013).

12. Burnap, R. L., Hagemann, M. & Kaplan, A. Regulation of CO<sub>2</sub> Concentrating Mechanism in Cyanobacteria. *Life* **5**, 348–371 (2015).
13. Spät, P., Barske, T., Maček, B. & Hagemann, M. Alterations in the CO<sub>2</sub> availability induce alterations in the phosphoproteome of the cyanobacterium *Synechocystis* sp. PCC 6803. *New Phytol.* **231**, 1123–1137 (2021).
14. Figge, R. M., Cassier-Chauvat, C., Chauvat, F. & Cerff, R. Characterization and analysis of an NAD(P)H dehydrogenase transcriptional regulator critical for the survival of cyanobacteria facing inorganic carbon starvation and osmotic stress. *Mol. Microbiol.* **39**, 455–469 (2001).
15. Klähn, S. *et al.* Integrated Transcriptomic and Metabolomic Characterization of the Low-Carbon Response Using an *ndhR* Mutant of *Synechocystis* sp. PCC 6803. *Plant Physiol.* **169**, 1540 (2015).
16. Jiang, Y.-L. *et al.* Coordinating carbon and nitrogen metabolic signaling through the cyanobacterial global repressor NdhR. *Proc. Natl Acad. Sci.* **115**, 403–408 (2018).
17. Omata, T., Gohta, S., Takahashi, Y., Harano, Y. & Maeda, S. Involvement of a CbbR Homolog in Low CO<sub>2</sub>-Induced Activation of the Bicarbonate Transporter Operon in Cyanobacteria. *J. Bacteriol.* **183**, 1891 (2001).
18. Nishimura, T. *et al.* Mechanism of low CO<sub>2</sub>-induced activation of the *cmp* bicarbonate transporter operon by a LysR family protein in the cyanobacterium *Synechococcus elongatus* strain PCC 7942. *Mol. Microbiol.* **68**, 98–109 (2008).
19. Selim, K. A., Haase, F., Hartmann, M. D., Hagemann, M. & Forchhammer, K. PII-like signaling protein SbtB links cAMP sensing with cyanobacterial inorganic carbon response. *Proc. Natl Acad. Sci.* **115**, E4861–E4869 (2018).
20. Liu, X.-Y. *et al.* Structures of cyanobacterial bicarbonate transporter SbtA and its complex with PII-like SbtB. *Cell Discov.* **7**, 1–5 (2021).
21. Fang, S. *et al.* Molecular mechanism underlying transport and allosteric inhibition of bicarbonate transporter SbtA. *Proc. Natl Acad. Sci.* **118**, e2101632118 (2021).
22. Maeda, S., Price, G. D., Badger, M. R., Enomoto, C. & Omata, T. Bicarbonate Binding Activity of the CmpA Protein of the Cyanobacterium *Synechococcus* sp. strain PCC 7942 Involved in Active Transport of Bicarbonate\*. *J. Biol. Chem.* **275**, 20551–20555 (2000).
23. Oldham, M. L., Khare, D., Quiocho, F. A., Davidson, A. L. & Chen, J. Crystal structure of a catalytic

- intermediate of the maltose transporter. *Nature* **450**, 515–521 (2007).
24. Korkhov, V. M., Mireku, S. A. & Locher, K. P. Structure of AMP-PNP-bound vitamin B12 transporter BtuCD–F. *Nature* **490**, 367–372 (2012).
  25. Sikkema, H. R. *et al.* Gating by ionic strength and safety check by cyclic-di-AMP in the ABC transporter OpuA. *Sci. Adv.* **6**, eabd7697 (2020).
  26. Caffalette, C. A. & Zimmer, J. Cryo-EM structure of the full-length WzmWzt ABC transporter required for lipid-linked O antigen transport. *Proc. Natl Acad. Sci.* **118**, e2016144118 (2021).
  27. Omata, T. Structure, Function and Regulation of the Nitrate Transport System of the Cyanobacterium *Synechococcus* sp. PCC 7942. *Plant Cell Physiol.* **36**, 207–213 (1995).
  28. Li, B. *et al.* Allosteric regulation of nitrate transporter NRT via the signaling protein PII. *Proc. Natl Acad. Sci.* **121**, e2318320121 (2024).
  29. Koropatkin, N. M., Pakrasi, H. B. & Smith, T. J. Atomic structure of a nitrate-binding protein crucial for photosynthetic productivity. *Proc. Natl Acad. Sci.* **103**, 9820–9825 (2006).
  30. Koropatkin, N. M., Koppenaar, D. W., Pakrasi, H. B. & Smith, T. J. The Structure of a Cyanobacterial Bicarbonate Transport Protein, CmpA\*. *J. Biol. Chem.* **282**, 2606–2614 (2007).
  31. Omata, T., Takahashi, Y., Yamaguchi, O. & Nishimura, T. Structure, function and regulation of the cyanobacterial high-affinity bicarbonate transporter, BCT1. *Funct. Plant. Biol.* **29**, 151–159 (2002).
  32. Du, J., Förster, B., Rourke, L., Howitt, S. M. & Price, G. D. Characterisation of Cyanobacterial Bicarbonate Transporters in *E. coli* Shows that SbtA Homologs Are Functional in This Heterologous Expression System. *PLOS ONE* **9**, e115905 (2014).
  33. Merlin, C., Masters, M., McAteer, S. & Coulson, A. Why Is Carbonic Anhydrase Essential to *Escherichia coli*? *J. Bacteriol.* **185**, 6415–6424 (2003).
  34. Davidson, A. L., Dassa, E., Orelle, C. & Chen, J. Structure, Function, and Evolution of Bacterial ATP-Binding Cassette Systems. *Microbiol. Mol. Biol. Rev.* **72**, 317–364 (2008).
  35. Rees, D. C., Johnson, E. & Lewinson, O. ABC transporters: the power to change. *Nat. Rev. Mol. Cell Biol.* **10**, 218–227 (2009).
  36. ter Beek, J., Guskov, A. & Slotboom, D. J. Structural diversity of ABC transporters. *J. Gen. Physiol.* **143**,

- 419–435 (2014).
37. Thomas, C. & Tampé, R. Structural and Mechanistic Principles of ABC Transporters. *Annu. Rev. Biochem.* **89**, 605–636 (2020).
38. Chovancova, E. *et al.* CAVER 3.0: A Tool for the Analysis of Transport Pathways in Dynamic Protein Structures. *PLOS Computational Biology* **8**, e1002708 (2012).
39. Buechel, E. R., Dimitrova, V. S., Karagiari, A., Kenney, L. G. & Pinkett, H. W. Structurally diverse C-terminal accessory domains in type I ABC importers reveal distinct regulatory mechanisms. *Structure* **33**, 843–857 (2025).
40. Gerber, S., Comellas-Bigler, M., Goetz, B. A. & Locher, K. P. Structural Basis of Trans-Inhibition in a Molybdate/Tungstate ABC Transporter. *Science* **321**, 246–250 (2008).
41. Kadaba, N. S., Kaiser, J. T., Johnson, E., Lee, A. & Rees, D. C. The High-Affinity *E. coli* Methionine ABC Transporter: Structure and Allosteric Regulation. *Science* **321**, 250–253 (2008).
42. Qiao, Z. *et al.* Structural insights into polyamine spermidine uptake by the ABC transporter PotD-PotABC. *Sci. Adv.* (2024).
43. Watzer, B. *et al.* The Signal Transduction Protein PII Controls Ammonium, Nitrate and Urea Uptake in Cyanobacteria. *Front. Microbiol.* **10**, (2019).
44. Lucius, S. & Hagemann, M. The primary carbon metabolism in cyanobacteria and its regulation. *Front. Plant Sci.* **15**, (2024).
45. Commichau, F. M., Forchhammer, K. & Stülke, J. Regulatory links between carbon and nitrogen metabolism. *Curr. Opin. Microbiol.* **9**, 167–172 (2006).
46. Muro-Pastor, M. I. & Florencio, F. J. Regulation of ammonium assimilation in cyanobacteria. *Plant Physiol. Biochem.* **41**, 595–603 (2003).
47. Kobayashi, M., Rodríguez, R., Lara, C. & Omata, T. Involvement of the C-terminal Domain of an ATP-binding Subunit in the Regulation of the ABC-type Nitrate/Nitrite Transporter of the Cyanobacterium *Synechococcus* sp. Strain PCC 7942\*. *J. Biol. Chem.* **272**, 27197–27201 (1997).
48. Herrero, A. & Flores, E. Genetic responses to carbon and nitrogen availability in *Anabaena*. *Environ. Microbiol.* **21**, 1–17 (2019).

- 
49. Thompson, R. F., Iadanza, M. G., Hesketh, E. L., Rawson, S. & Ranson, N. A. Collection, pre-processing and on-the-fly analysis of data for high-resolution, single-particle cryo-electron microscopy. *Nat. Protoc.* **14**, 100–118 (2019).
  50. Punjani, A., Rubinstein, J. L., Fleet, D. J. & Brubaker, M. A. cryoSPARC: algorithms for rapid unsupervised cryo-EM structure determination. *Nat. Methods* **14**, 290–296 (2017).
  51. Zheng, S. Q. *et al.* MotionCor2: anisotropic correction of beam-induced motion for improved cryo-electron microscopy. *Nat. Methods* **14**, 331–332 (2017).
  52. Rohou, A. & Grigorieff, N. CTFFIND4: Fast and accurate defocus estimation from electron micrographs. *J. Struct. Biol.* **192**, 216–221 (2015).
  53. Scheres, S. H. W. Amyloid structure determination in RELION-3.1. *Acta Crystallogr. D Struct. Biol.* **76**, 94 (2020).
  54. Kucukelbir, A., Sigworth, F. J. & Tagare, H. D. Quantifying the local resolution of cryo-EM density maps. *Nat. Methods* **11**, 63–65 (2014).
  55. Emsley, P. & Cowtan, K. Coot: model-building tools for molecular graphics. *Acta Crystallogr. D Biol. Crystallogr.* **60**, 2126–2132 (2004).
  56. Waterhouse, A. *et al.* SWISS-MODEL: homology modelling of protein structures and complexes. *Nucleic Acids Res.* **46**, W296–W303 (2018).
  57. Pettersen, E. F. *et al.* UCSF ChimeraX: Structure visualization for researchers, educators, and developers. *Protein Sci.* **30**, 70–82 (2021).
  58. Adams, P. D. *et al.* PHENIX: a comprehensive Python-based system for macromolecular structure solution. *Acta Crystallogr. D Biol. Crystallogr.* **66**, 213 (2010).
  59. Williams, C. J. *et al.* MolProbity: More and better reference data for improved all-atom structure validation. *Protein Sci.* **27**, 293–315 (2018).
  60. Kabsch, W. XDS. *Acta Crystallogr. D Biol. Crystallogr.* **66**, 125–132 (2010).
  61. Murshudov, G. N., Vagin, A. A. & Dodson, E. J. Refinement of Macromolecular Structures by the Maximum-Likelihood Method. *Acta Crystallogr. D Biol. Crystallogr.* **53**, 240–255 (1997).
  62. Winn, M. D. *et al.* Overview of the CCP4 suite and current developments. *Acta Crystallogr. D Biol.*

---

*Crystallogr.* **67**, 235–242 (2011).

63. Graef, J., Ehrt, C. & Rarey, M. Binding Site Detection Remastered: Enabling Fast, Robust, and Reliable Binding Site Detection and Descriptor Calculation with DoGSite3. *J. Chem. Inf. Model.* **63**, 3128–3137 (2023).
64. Feng, J. *et al.* An improved malachite green assay of phosphate: Mechanism and application. *Anal. Biochem.* **409**, 144–149 (2011).

ARTICLE IN PRESS

---

## Acknowledgments

We thank Dr. Yong-Xiang Gao at the Center for Integrative Imaging, University of Science and Technology of China for his assistance with cryo-EM image acquisition. This work was supported by the National Natural Science Foundation of China (32401040 to S.-J.H., 32241025 to C.-Z.Z., and 32171198 to Y.-L.J.), the Anhui Provincial Key Research and Development Project (2022107020034 to Y.-L.J.), the Natural Science Foundation of Anhui Province (2408085QC088 to R.-Q.Z.), and the USTC Research Funds of the Double First-Class Initiative (YD9100002023 to Y.-L.J.).

## Author Contributions

Y.-L.J., C.-Z.Z., Y.C. and W.-T.H. conceived, designed, and supervised the project. Y.-L.J., C.-Z.Z., Q.-Y.L., B.L., R.-Q.Z. and S.-J.H. analyzed the data and wrote the manuscript. Q.-Y.L. and B.L. performed the molecular cloning, protein expression, purification, crystallization, cryo-EM samples preparation and biochemical assays. Q.-Y.L., B.L. and Y.-L.J. performed the data collection, structure determination and model building. Q.-Y.L., B.L. and R.-Q.Z. performed the physiological experiments. J.-L.L. constructed the *E. coli* C43- $\Delta can$  strain. All authors discussed the data and read the manuscript.

## Competing interests

The authors declare no competing interests.

## Figure Legends

### Fig. 1 | Sequence alignment of CmpC-CRD homologs and crystal structures of CmpC-CRD.

**a** Multiple sequence alignment of residues in the substrate-binding pockets of cyanobacterial CmpC-CRD, NrtC-CRD, and NrtA homologs. The substrate-binding residues are marked by black and red circles. **b** Isothermal titration calorimetry analysis of CRD binding to nitrate. The upper panel shows the raw ITC data in the form of the heat produced during the titration. The lower panel shows the binding isotherms and the best-fit curve based on the one-set-of-sites model. **c** Crystal structure of apo-CRD. The lobe I, lobe II, and the C-terminal subdomain are colored in yellow, green, and orange, respectively. **d** Crystal structure of nitrate-bound CRD and a zoomed-in view highlighting the residues involved in nitrate binding in the crystal structure. The nitrate molecule is shown as sticks with  $2F_o - F_c$  electron density contoured at  $2\sigma$  shown as a blue mesh. The subdomains are colored as in the apo-CRD structure. The residues interacting with nitrate are shown as sticks and labeled.

### Fig. 2 | Bicarbonate uptake activity assays of CmpABCD.

**a** Dilution spotting assays of CmpABCD and mutants in *E. coli* C43 strains. The wild-type strain served as the positive control, and the *E. coli* C43- $\Delta can$  strain with an empty vector served as the negative control. CmpABCD, CmpABC $\Delta CRD$ D and CmpABC<sub>R315A</sub>D<sub>E255Q</sub> from *Pseudanabaena* sp. Chao 1811 were expressed in the *E. coli* C43- $\Delta can$  strains. **b** Bicarbonate uptake activity assays in *Synechocystis* sp. PCC 6803. WT: wild-type; CmpC $\Delta CRD$ : deletion of *cmpC-CRD*. Uptake assays were performed by adding 100  $\mu\text{M}$   $\text{H}^{14}\text{CO}_3^-$  to the cell suspensions and incubating for 2 min. The relative uptake activity of each mutant was normalized by WT. Each experiment was conducted in triplicate, represented by dark data points. Error bars indicate the means  $\pm$  standard deviation (SD). Statistical significance was determined using unpaired, two-sided *t* tests. The *P* value of CmpC $\Delta CRD$  is 0.0183;  $*P < 0.05$ . Source data are provided as a Source Data file.

### Fig. 3 | Cryo-EM structure of apo-CmpBCD and bicarbonate uptake activity of CmpABCD in *Synechocystis* sp. PCC 6803.

**a** Cartoon representation of apo-CmpBCD structure. The red triangle marks the region encompassing the centers of the two NBDs and the CRD. **b** Local resolution distribution of the final reconstruction of apo-CmpBCD. **c** Interface between CmpC-NBD and CmpC-CRD, colored as in the apo-CmpBCD. The residues involved in the interactions are shown as ball-and-stick models. The meshes of these residues are colored in blue with contour levels set at  $\sigma=5$ . The salt bridges and hydrogen bonds are shown with dashed lines. **d** Interface between CmpD and CmpC-CRD with segments colored as in the apo-CmpBCD. The residues involved in the interactions are shown as ball-and-stick models. The meshes of these residues are colored in blue with contour levels set at  $\sigma=5$ . The salt bridges and a hydrogen bond in the interface are shown with dashed lines. **e** Bicarbonate uptake activity in *Synechocystis* sp. PCC 6803. WT: wild-type; CmpC<sub>R315A</sub>&CmpD<sub>E257Q</sub>: double mutations of CmpC<sub>R315A</sub> and CmpD<sub>E257Q</sub>. The bicarbonate uptake assays were performed by adding 100  $\mu\text{M}$   $\text{H}^{14}\text{CO}_3^-$  to the cell suspensions and incubating for 2 min. The uptake activity of mutant was normalized by WT. Each experiment was conducted in triplicate, represented by dark data points. Error bars indicate the means  $\pm$  SD. The statistical significance was determined using unpaired, two-sided *t* tests. The *P* value of CmpC<sub>R315A</sub>&CmpD<sub>E257Q</sub> is 0.0024;  $**P < 0.01$ . Source data are provided as a Source Data file.

**Fig. 4 | Bicarbonate uptake activities of CmpABCD and Cryo-EM structure of CmpBCD in the presence of NO<sub>3</sub><sup>-</sup> (CmpBCD-NO<sub>3</sub><sup>-</sup>).** **a** Bicarbonate uptake activity in wild-type *Synechocystis* sp. PCC 6803 cultured in the presence of different nitrogen sources: NO<sub>3</sub><sup>-</sup> and NH<sub>4</sub><sup>+</sup>. **b** Bicarbonate uptake activity in *Synechocystis* sp. PCC 6803. WT: wild-type; CmpC<sub>K482A</sub>: single mutation of CmpC-CRD Lys482 to alanine. **(a, b)** Uptake assays were performed by adding 100 μM H<sup>14</sup>CO<sub>3</sub><sup>-</sup> to the cell suspensions and incubating for 2 min. The uptake activities of WT cultured in the presence of NH<sub>4</sub><sup>+</sup> and the mutant are normalized by WT cultured in the presence of NO<sub>3</sub><sup>-</sup>. Each experiment was conducted in triplicate, represented by dark data points. Error bars indicate the means ± SD. The statistical significance was determined using unpaired, two-sided *t* tests; \*\*\*\**P* < 0.0001. Source data are provided as a Source Data file. **c** Local resolution distribution of the final reconstruction of CmpBCD-NO<sub>3</sub><sup>-</sup>. **d** Structural superposition of CmpBCD-NO<sub>3</sub><sup>-</sup> (slate) and apo-CmpBCD (gray). All α-helices are displayed as cylinders. The hinge helix of CmpBCD-NO<sub>3</sub><sup>-</sup> is colored red. The hinge helices of the two structures rotate by ~20°.

**Fig. 5 | Cryo-EM structure of CmpBCD-ATP.** **a** Cartoon representation of the CmpBCD-ATP structure. The subunits are colored as in apo-CmpBCD. Two ATP molecules are shown as sticks and two Mg<sup>2+</sup> ions are shown as spheres in green. **b** Structural superposition of TMDs in CmpBCD in the presence of NO<sub>3</sub><sup>-</sup> (gray) and CmpBCD-ATP (violet and slate). All α-helices are displayed as cylinders. ATP binding drives NBD dimer closure, which promotes the rearrangements of TMDs, reducing the distance between the two coupling helices from 25.4 Å to 13.3 Å. The two TM5 helices in the outer membrane leaflet undergo an outward shift of 10.9° relative to the central axis. The distances between the two coupling helices and the shift angle of TM5 helices in the two structures are shown.

**Fig. 6 | A proposed regulatory model of CmpABCD.** The CmpABCD is shown as the schemes, with the subunits and domains colored differently. Under high C/N level with limited nitrate, the apo-CRD binds two NBDs and locks CmpABCD in an auto-inhibited conformation, blocking the bicarbonate transport. Under low C/N level with abundant nitrate, CRD binding to nitrate releases from the NBDs and restores the bicarbonate transport activity of CmpABCD. The transport cycle starts from the resting state with the TMDs adopting an inward-facing conformation. Upon the docking of substrate-loaded CmpA to TMDs (pre-translocation state), ATP binding to NBDs triggers a structural transition of the importer from an inward-facing to an occluded and subsequently an outward-facing conformation. Following ATP hydrolysis, the NBDs partially separate, facilitating the return to the inward-facing state and the release of substrate. The resting, pre-translocation, and outward-facing states, which were not observed in this study, are marked with blue dashed boxes. The gradient of C/N condition is represented by a blue scale bar at the bottom. Adapted from [Li, B. *et al.* Allosteric regulation of nitrate transporter NRT via the signaling protein PII. *Proc. Natl Acad. Sci.* **121**, e2318320121 (2024)]<sup>28</sup>, CC BY-NC-ND 4.0 (<https://creativecommons.org/licenses/by-nc-nd/4.0/legalcode.en>).

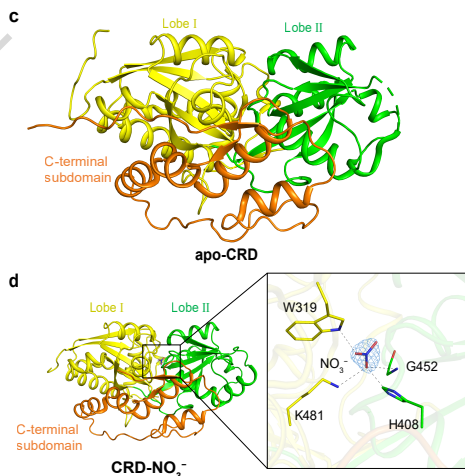
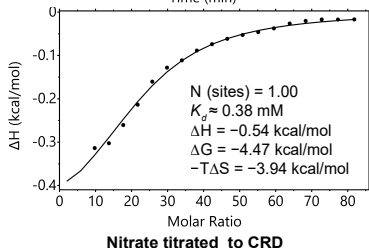
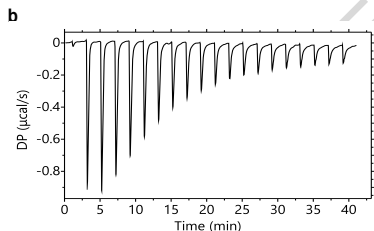
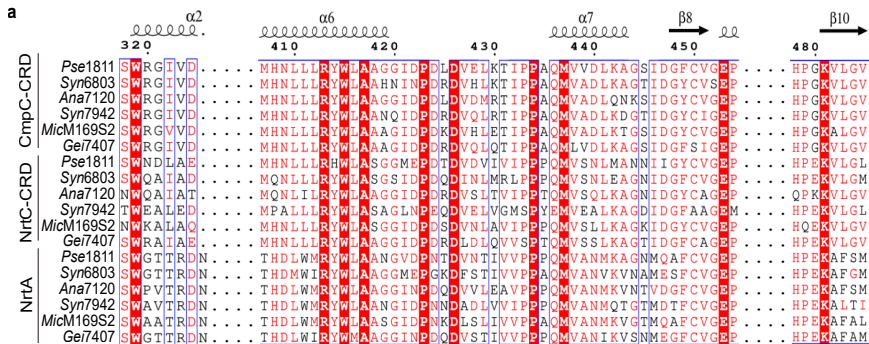
---

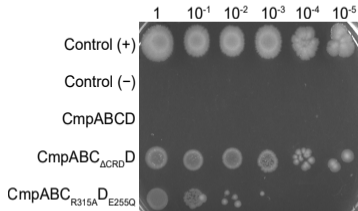
**Editorial Summary:**

Carbon and nitrogen uptake should be coordinated to maintain metabolic balance in cyanobacteria. Here, authors reveal how the bicarbonate importer CmpABCD is activated by intracellular nitrate, uncovering a structural mechanism that directly links carbon uptake to nitrogen availability.

**Peer review information:** *Nature Communications* thanks Karl Forchhammer and the other, anonymous, reviewer(s) for their contribution to the peer review of this work. A peer review file is available.

ARTICLE IN PRESS



**a****b**